Layering transitions in colloidal crystals as observed by diffraction and direct-lattice imaging

David H. Van Winkle and C. A. Murray
AT&T Bell Laboratories, Murray Hill, New Jersey 07974
(Received 31 January 1986)

Layering transitions of colloidal crystals confined between two smooth glass surfaces have been studied by transmission diffraction of light as well as direct-lattice imaging with an optical microscope. The polystyrene spheres we studied have diameter $\Phi=0.305$ μm and a surface charge of $\sim 10^4$ electronic charges, and form three-dimensional (3D) colloidal crystals in completely deionized water at a volume concentration above $\approx 0.3\%$. A 3D suspension of these spheres in completely deionized water forms both body-centered-cubic (bcc) and face-centered-cubic (fcc) crystalline structures as a function of colloid density $n \equiv (1/a_s)^3$, with lattice constants ranging between 0.7 and 1.5 μm. When the colloid is confined between glass plates separated by distances $D \sim 0.5-1$ μm, the spheres form a single-layer 2D fluid. For D near 1 μm, a transition occurs to a single-layer 2D hexagonal crystal. As D increases, the evolution from two- to three-dimensional crystals is observed as a series of structural transitions distinguished by the number of crystal planes between the plates and by the preferred crystal symmetry parallel to the glass boundaries. We present here a study of colloidal crystals confined in a wedge cell that allows diffraction and imaging from the same crystallite. We present diffraction and imaging measurements of structural phases of one- through seven-layer colloidal crystals confined between two smooth glass surfaces, for a range of densities such that $2 < a_s/\Phi < 6$. The sequence of structural phases we observe for this range of densities for clean samples is similar but not identical to that observed for $a_s/\Phi < 2$ by Pieranski, Strzlecki, and Pansu, which was modeled as a hard-sphere system. We also observe differences between the clean thin crystalline phases and "dirtier" thin phases to which a stray electrolyte has been added. The use of both diffraction and imaging was found necessary to fully characterize the system.

I. INTRODUCTION

Colloidal spheres in very clean water comprise a system of fundamental physical interest.[1,2] A wide variety of polystyrene latex spheres that range in diameter from 0.1 to 1 μm, and surface charge between $\sim 10^3$ and 10^5 electron charges are now commercially available[3] with dispersion of both sphere diameter and surface charge as small as 1–3%.[4] A colloidal suspension of polystyrene sulfonate latex spheres in a water electrolyte can be considered, to first approximation, a monodisperse system of highly charged spheres of diameter Φ and charge Ze interacting by repulsive Coulomb forces at large interparticle separation. Dissociation of potassium sulfonate groups from the surface of each sphere when it is dispersed in water produces the sphere charge, and also Z potassium counterions per sphere. These counterions can be exchanged with hydronium ions supplied by ion-exchange resin. The resulting counterions and other added electrolytes in the water serve to screen the sphere-sphere Coulomb interactions in a classical analogy to an electron screening cloud around an ion in a cold plasma or metal. When a suspension of spheres is confined in three dimensions (3D) in very clean deionized water, it can form structures exactly analogous to fluid and solid phases of atomic systems. Depending on the colloid used, solids with interparticle separations as large as 2 μm may be formed. The size scale makes the colloidal system quite amenable to study with visible light, via both diffraction[5] and "atomic resolution" microscopic imaging.[6]

A simplified picture of the basic physics of the colloidal system can be obtained by considering two hypothetical limits of the relevant parameters that govern the physics of interaction. Neglecting the vary narrow and deep first Van der Waals minimum in the Derjaguin-Landau-Verwey-Overbeek (DLVO) interaction potential between two spheres as a function of their mutual separation [reasonable for large separations of spheres of high surface charge (Ref. 7)] the primary interaction between the spheres is repulsive Coulomb in nature. Consider a 3D collection of identical spheres of diameter Φ and charge Ze in a background of Z-point screening ions of charge e, held at constant temperature T and density n. This model system can be characterized by the length, λ, of the spatial decay of the screening cloud around each sphere as well as the average sphere separation $a_s \equiv (1/n)^{1/3}$. The parameters of the system can be expressed as ratios of the three relevant lengths: a_s/Φ and a_s/λ. In the limit of high density and very short spatial decay of the screening, or $a_s/\Phi \simeq 1$, and $a_s/\lambda \gg 1$, the system acts like a collection of hard spheres. In the opposite limit of large sphere separation and very long decay of the screening, or $a_s/\Phi \gg 1$ and $a_s/\lambda \ll 1$, the system acts like a classical one-component plasma (OCP) of point charges in a uni-

form background of neutralizing charge.

By adjusting appropriate experimental parameters, the colloidal system may be moved within the phase space between the two limiting models, never attaining either. Both the classical hard-sphere system[8] and the OCP system[9] have been extensively studied by molecular dynamics and Monte Carlo simulations. The hard-sphere phase diagram in 3D can be characterized by the reduced pressure $p \equiv P/nk_BT$ and a single parameter, a_s/Φ, where k_B is the Boltzmann factor and P is the pressure. The system melts from a close-packed solid [either fcc or hexagonal close packed (hcp)] only as a function of a_s/Φ. There is a very small two-phase coexistence region for $0.98 < a_s/\Phi < 1.02$, and the system undergoes a first-order phase transition to a fluid for $a_s/\Phi > 1.02$. The classical OCP can be characterized by a single parameter $\Gamma = Ze/r_s k_B T$, where $r_s \equiv (4\pi/3)^{-1/3} a_s$. In 3D, the OCP undergoes a first-order melting transition from a bcc crystal at large Γ to a fluid at $\Gamma \leq 155$. The colloid system is intermediate between the two limits, and is characterized by two ratios, a_s/Φ and a_s/λ. As in the case of the limiting systems, the temperature of the colloid can be scaled into the parameters (in this case λ). Changing the temperature of a colloidal suspension alters a great many things,[10,11] such as the dielectric constant of the water and various dissociation rates of the water, the walls of the container, the ion-exchange resin used to clean the colloid, and the colloid itself. In order to observe a continuous and controlled change in chemical potential we leave the system at a constant temperature and vary either sphere density (a_s and λ) or electrolyte concentration (λ). Changing these parameters effectively varies the ratio of the sphere-sphere interaction energy to (fixed) temperature. As a function of the relevant experimentally accessible parameters, the colloid system can undergo a continuous transformation between the two limiting cases of hard spheres and OCP. The rich physics of the colloid system in 3D has not yet been completely understood, and is currently a subject of great interest.[2]

For a colloid system confined between two smooth repelling plates, separated by an adjustable distance D, structural phases differing from those observed in bulk will form. Glass surfaces repel the colloidal spheres for two reasons: They are highly charged in water, with a density of OH^- groups approaching 2.5×10^{14} cm^{-2},[12] a charge density comparable to that on the sphere surfaces. In addition, there exist repulsive image charges of the spheres, due to the dielectric constant variation across the water-glass interface, from 80 (water) to 5 (glass). Both real and image charges on the glass are the same sign as that on the spheres. When a deionized high-density colloid system is confined between glass plates, only an integral number of crystalline layers may exist in equilibrium. As a consequence, an infinite series of layering transitions is observed from a single layer 2D crystal to bulk 3D crystals. Pansu *et al.*[1] have reported studies of these layering transitions for 1.1 μm diameter polystyrene spheres close to the hard-sphere limit. For the large spheres they studied, with $1.4 < a_s/\Phi < 1.9$, they observed a sequence of structural phases identical to that expected for hard-sphere systems at high density.[13] At the high-pressure limit, hard spheres confined between two infinitely repulsive parallel flat surfaces undergo the following series of structural transitions: vac$-1\triangle-2\square-2\triangle-3\square-3\triangle-\cdots-N\triangle-(N+1)\square-(N+1)\triangle-\cdots$ where vac represents vacuum, and the other symbols represent the number of layers and the crystal symmetry (hexagonal or square) parallel to the confining surfaces. These structures maximize the sphere density for a given separation between the plates, leading naturally to a new parameter a_s/D.

We studied the structures occurring for a colloidal system spanning the range of relevant parameters that produce both fcc and bcc crystals in 3D changing the location in phase space between the hard-sphere and OCP limits. We find a sequence of layering transitions in our colloidal system that is similar, but not identical to the sequence listed above for hard spheres. The cleanliness of our experimental system allows studies of these transitions for $2 < a_s/\Phi < 6$. We see distinct stability differences between the $\triangle$ and $\square$ structures, and only hcp stacking symmetry for the $\triangle$ phases for small number of layers N at low densities. We find a gradual distortion of the $\square$ phases above about four layers to a structure with the symmetry of a bcc $\langle 110 \rangle$ face parallel to the glass boundaries. The intermediate "hopping" regions found between the $1\triangle$ and $2\square$ structures[1,14] are much more pronounced in our system, and we see them for other $N\triangle-(N+1)\square$ transitions. These are regions of intense correlated vertical-sphere motion between two or more end positions that are especially evident between the $1\triangle$ and $2\square$ structures. Finally, the cell we have designed allows the study of ten to a hundredfold smaller wedge angles ($\sim 10^{-4}$ rad) than previous experiments, with the combination of both diffraction and imaging studies of the same location. Thus the crystallite sizes we studied are considerably larger in lateral dimension, on the order of 500 to 1000 lattice constants for the $1\triangle$ phase, and we are able to observe subtle changes in the diffraction pattern of each structure as its thickness varies that are not possible to resolve experimentally by imaging.

We report studies of structural transitions using both light diffraction and imaging from the same crystallites. These two techniques give both different and complementary information about the structure of the system: Diffraction gives information on the long-range crystalline order as well as the crystalline symmetry, but is a poor technique for learning about short-range order or disordered systems. Essential phase information is lost upon taking the Fourier transform of the diffraction pattern to obtain the pair-correlation function of a system, therefore one can only deduce the real-space positions of atoms, with a nonunique solution. Real-space imaging is a very powerful technique for determining the actual positions of atoms in either a crystalline or disordered structure, if atomic resolution "snapshots" of the system can be obtained. Much excitement has been generated by the extremely powerful atomic scale Angstrom resolution electron microscopy[15] and vacuum tunneling microscopy[16] techniques that have recently been developed. They are capable, for the first time, of uniquely determining the positions of real atoms in complicated problems such as sur-

face reconstructions. To explore in one system both the long-range crystalline symmetries and the short-range structure requires the use of both diffractive and imaging techniques.

In the colloidal system, "atomic scale" resolution snapshots of the system can be taken with ease, using ordinary visible light and high-powered light microscopes. This is possible due to the ~ 1 μm spatial scale and the ~ 1 msec time-scale[17] characteristic of the colloid. The wavelength of light in the colloid medium is roughly 0.3 μm, comparable to the diameter of our polystyrene spheres, and at high sphere densities, comparable to their separation as well. Thus the light microscope used must be diffraction limited in its optics, and yields a diffractive imaging situation similar to that of the actual atomic resolution electron-microscope technique[15]. In the experiment we describe here, for values of the parameter a_s/Φ ranging between 2 and 6, we can easily step through the crystal, focusing layer by layer with few complications associated with the diffractive nature of the imaging. We are limited in the vertical resolution of the imaging technique, however, by the depth of focus of the objective, which is ± 0.2 μm, and eventually by multiple scattering, which reduces the contrast as one steps through many layers of the colloid. The imaging technique is very powerful for determining short-range structure in the system, and the actual position of each "atom."

II. EXPERIMENTAL TECHNIQUES

A. Cell and colloid

To investigate regimes with a_s/Φ as large as 6 requires a very clean colloid reservoir, stable against external environmental contamination. The design of our cylindrical, 180-mm-diameter, $\approx$30-mm-high cell enabling both light diffraction and imaging of the same colloidal crystal is illustrated in Fig. 1. The experimental area of the cell is in the center, bordered on top by a 25-mm-diameter fused silica optical flat (flatness $\lambda/20$) and at the bottom by a 25-mm diameter, 0.15-mm-thick cover slip. The separation between the two windows is controlled by three differential micrometers and measured by three linear variable difference transducers. The body of the cell is oxygen-free high-conductivity (OFHC) copper electroplated with 25 μm of hard gold and 25 μm of soft gold[18] The inner surfaces of the cell were freon vapor degreased before final assembly leaving a clean gold surface, which does not release ions when in contact with the colloidal solution. Cleaned ion-exchange resin[19] is placed in 70 μm mesh nylon torroidal bags which encircle the experimental area at three different radii. Teflon and nalgene plumbing is used to load the colloid into the cell and seal it from the environment. A conductivity meter is sealed in the cell in contact with the 100-ml reservoir of colloid which surrounds the experimental area. The conductivity of the 3D colloid reservoir is used to monitor the system cleanliness and check for possible air leaks into the cell. The coverslip is glued with Epotek 302, a water-resistant epoxy, into a removable tantalum flange which is sealed by neoprene O rings onto the bottom plate of the cell. The entire cell is also sealed by a large neoprene O ring,

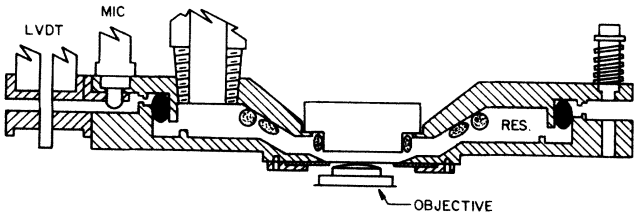

FIG. 1. Schematic drawing of the experimental cell. Cell body is machined of OFHC copper and electroplated with gold. Observation area is in the center, shown with thickness D as large as possible. Cell is sealed by a $\sim$12-cm-diameter neoprene O ring, depicted as black ovals in this cut-away drawing. Upper surface of the experimental area is a $\lambda/20$ optical flat and the lower surface a microscope slide cover slip of diameter 2.5 cm and thickness ~ 150 μm. Observation region between the windows may be closed to zero thickness, and opened to 3 mm. A wedge between the windows can be formed by bowing the thin lower window by pumping slightly on the teflon cell-fill lines, one of which is shown at top left. Cell is opened and closed with the use of three differential micrometers (MIC), and the opening is measured by three linear variable displacement transducers (LVDT), located at 120° around the outside diameter of the cell. Surrounding 3D colloid reservoir (RES) contains three torroidal bags of ion-exchange resin (dotted ovals) and $\approx$100 ml of colloidal solution. Imaging is performed with a 140X, numerical aperture 1.3, oil-immersion objective in reflection geometry as shown. Cell is removed from the microscope and a laser beam is steered into the cell at any angle through the bottom window to produce diffraction patterns on a translucent screen placed on top of the upper window.

and may be opened more than 3 mm without leaking. The top of the coverslip extends above the surface of the flange which holds it, and the bottom of the optical flat extends below the bottom of the cell base when the cell is fully closed. This allows closing of the gap between the two optical surfaces. By adjusting the micrometers it is possible to obtain thickness uniformity of ± 2 μm across the 2.5-cm-diameter experimental area at thicknesses ranging between 0 and 10 μm. The cell provides an environment, stable for months, in which thin colloidal structures may be studied by both diffraction and imaging.

Care must be exercised in preparing the colloid and loading it into the cell to obtain good crystallites at large a_s/Φ. The polystyrene latex spheres were obtained from Dow Corning and were characterized by them as 0.3050 ± 0.0084 μm diameter. They were premixed with very clean distilled and deionized water at the desired weight percentage, and allowed to sit in a sealed nalgene container for several weeks in direct contact with mixed-bed H^+ and OH^- ion-exchange resin, to allow for electrolyte exchange. An estimate of the sphere surface charge of $Z = (4 \pm 1) \times 10^4$ was obtained by measuring the cleaned solution pH at several different colloid volume fractions. Preparation and transfer of the colloidal solution is performed in a sealed nitrogen-gas atmosphere, to minimize the introduction of both carbonate ions and dust particles into solution from the air. The cell is assembled using a thick glass bottom window allowing use of pressures close

to 1 atm for loading the colloid into the cell through a 70-μm mesh filter. After the cell is filled with colloid, its bottom window is replaced with the thin cover slip. For studying the layering transitions, we create a smooth wedge as small as 10^{-4} rad between the two cell windows by first closing the cell to $D \sim 10$ μm thickness and then bowing the cover slip up to the optical flat by pumping slightly on the cell-fill plumbing. In roughly five days, excess ions trapped between the plates diffuse to the first resin bag and the colloid crystallizes. The crystallites that form typically span from 100 μm—1 mm in lateral linear dimension.

For much of the low-density (large a_s/Φ) data reported in this paper, small teflon cells were used to hold the colloid in a fixed wedge geometry for imaging only. These machined cylindrical cells have 2 cm inner diameter and are 4 cm high, holding up to ~ 30 ml of colloid between two glass windows sealed to their top and bottom surfaces with neoprene O rings. The fixed wedge was formed by the addition of a 1-cm diameter, 0.3-cm-thick fused silica optical flat to the cell before colloid filling. The small optical flat was laid on top of the clean bottom cell window in a clean environment. Unavoidable dust particles on the window created a natural wedge of 10^{-2}—10^{-3} rad between the window and one edge of the optical flat. Precleaned colloid was then loaded into the cell in a nitrogen atmosphere and was wicked by surface tension under the optical flat into the wedge. To maintain cleanliness of the colloid, a bag of 70-μm nylon mesh containing ~ 2 ml of mixed-bed ion-exchange resin was placed directly on top of the small optical flat, in direct contact with the bulk solution of colloid. The colloid then crystallized in about two days. Several of these small cells are still crystallized one year after filling.

B. Diffraction

A spatially filtered argon-ion laser beam with a 25-μm-diameter focal-spot size is used to study diffraction from the colloid. The beam is steered along the axis of rotation of a mechanical rotation stage coplanar with the cell bottom window, enabling a 2θ scan about this axis for any particular crystallite of interest. The laser beam is first directed along the mechanical stage rotation axis and then up into the cell from below, using beam steering optics mounted on a swinging arm. It eventually passes into the colloid through the thin bottom cell window. After alignment of the optics, rotation of the incident beam angle θ causes less than 25-μm lateral displacement of the beam in the window plane. The incident beam direction θ can be varied between $\pm 65°$ from normal to the window. The cell may be translated by micrometers and rotated in the plane parallel to the window. The cell is mounted successively on an XY translation stage, a rotation stage, and another XY translation stage. The cell rotation stage provides the ϕ scan of the crystal, about an axis normal to the window plane. The lower-level XY translators allow intersection of the ϕ axis of rotation with the 2θ axis of rotation. The upper XY translators move different crystallites into the chosen scattering point. One may observe either forward or back scattering from the crystal, with a limit of 65° from normal to the sample in back scattering and 60° from normal in forward scattering. Forward diffraction passes through the 16.5-mm-thick fused silica top cell window, and is recorded by photographing the diffraction pattern obtained on a thin frosted mylar flat-sheet diffuser placed on the window top surface. Back diffraction is only particularly useful when the sample is so thick that forward diffraction is washed out by multiple scattering. The thickest crystal from which we have been able to observe forward scattering is ~ 500 μm. The diffraction measurements reported here were obtained in forward scattering from the big copper cell by translating the cell in the focused laser beam so that the beam traversed a line of increasing colloid thickness parallel to the wedge between the two windows. In order to do real-space imaging of the identical region in the cell, the position of the starting and end points of the diffraction run were recorded relative to the center of the cell and the sample immediately moved to the microscope translation stage for imaging.

C. Imaging

We use a Reichert MeF metallurgical microscope for imaging the colloidal crystals in reflection through the bottom cover slip of either the big copper or small teflon cells, using a 140X, numerical aperture 1.3, oil-immersion objective with depth of focus ± 0.2 μm. The working distance of the objective is ≈ 250 μm, so that the bottom windows of the cells must be thinner. We used cover slips that are ≈ 150 μm thick with variation in thickness over their 25-mm diameter of less than ten wavelengths of green light. The microscope source of illumination is a Xenon arc lamp, filtered by ≈ 8 orders of magnitude for light wavelengths below 1 μm in the infrared, and also for wavelengths above 0.3 μm in the ultraviolet. The reflected image of the colloid may be viewed either through the microscope eyepiece, or through a side port with a video camera or with a charged-coupled-device (ccd) camera for digitizing the images. The cell position relative to the objective is determined by the micrometer driven XY translation stage of the microscope, which is calibrated with respect to the translation stages of the diffraction optics.

To calibrate the relative positions of the cell on the two experimental stages for diffraction and imaging, we used a 25-μm-diameter pinhole, mounted such that when placed on the diffraction stage or on the microscope stage it would be in the same plane as the cell bottom window. We are able to reproducibly duplicate position on the diffraction stage within ± 15 μm. The reproducibility of pinhole position on the microscope stage is ± 25 μm. Reproducibility of the cell position on the diffraction stage is comparable to that of the pinhole, whereas on the microscope, picking up and replacing the cell can shift the relative position of the microscope objective by as much as 500 μm. This was monitored by finding either small scratches or characteristic pieces of dirt 10—30 μm in lateral dimension attached to one or the other window, so that corrections could be made as necessary. These methods are sufficient to find exactly the same crystallite to within the focal-spot size of the laser for both diffrac-

tion and imaging.

Measurement of crystal lattices and densities are made by using either the video or the ccd imaging systems. The two cameras are mounted on separate optical rails on the microscope so that they can be individually translated away from the objective lens. The power of the objective is sufficiently high that effective magnification of the colloid image on either camera chip can easily by increased by moving the camera a few inches away from the objective, and adjusting the microscope focus by a few μm (the image formed by the objective is with an $f/40$ cone). In this way, we can adjust the total number of spheres recorded in a single image up to the chip resolution limit. The planar (XY) distance scale of the image on the camera chips is calibrated by comparison to the image of a set of electron-beam written lines on glass with 2-μm spacing between centers. We estimate the accuracy of measuring planar lattice spacings in the colloid to be roughly 2% for spacings of 10 pel or more on either of the camera chips. The calibration of the vertical (Z) distance scale of the microscope is more difficult due to the unknown and changing index of refraction of the colloid as a function of the thickness probed, as well as the depth of focus of the lens, 0.2 μm. We used the vertical layer spacing of well-stabilized, defect free regions of 3D fcc and bcc colloid crystals formed in a small teflon cell from similar density 0.305-μm-diameter polystyrene spheres as an internal standard of vertical distance. Ten measurements of crystal layer spacings were made for the first 17 layers next to the bottom-cell-window top surface and averaged together to obtain the calibration, using the measured horizontal lattice parameter of the crystals to obtain the expected layer spacings.

In the present experiment, we measured the colloid thickness in the wedge by focusing on the top surface of the bottom window and then translating the objective vertically until the bottom surface of the glass plate forming the top of the wedge came into focus. A 10:1 reduc-

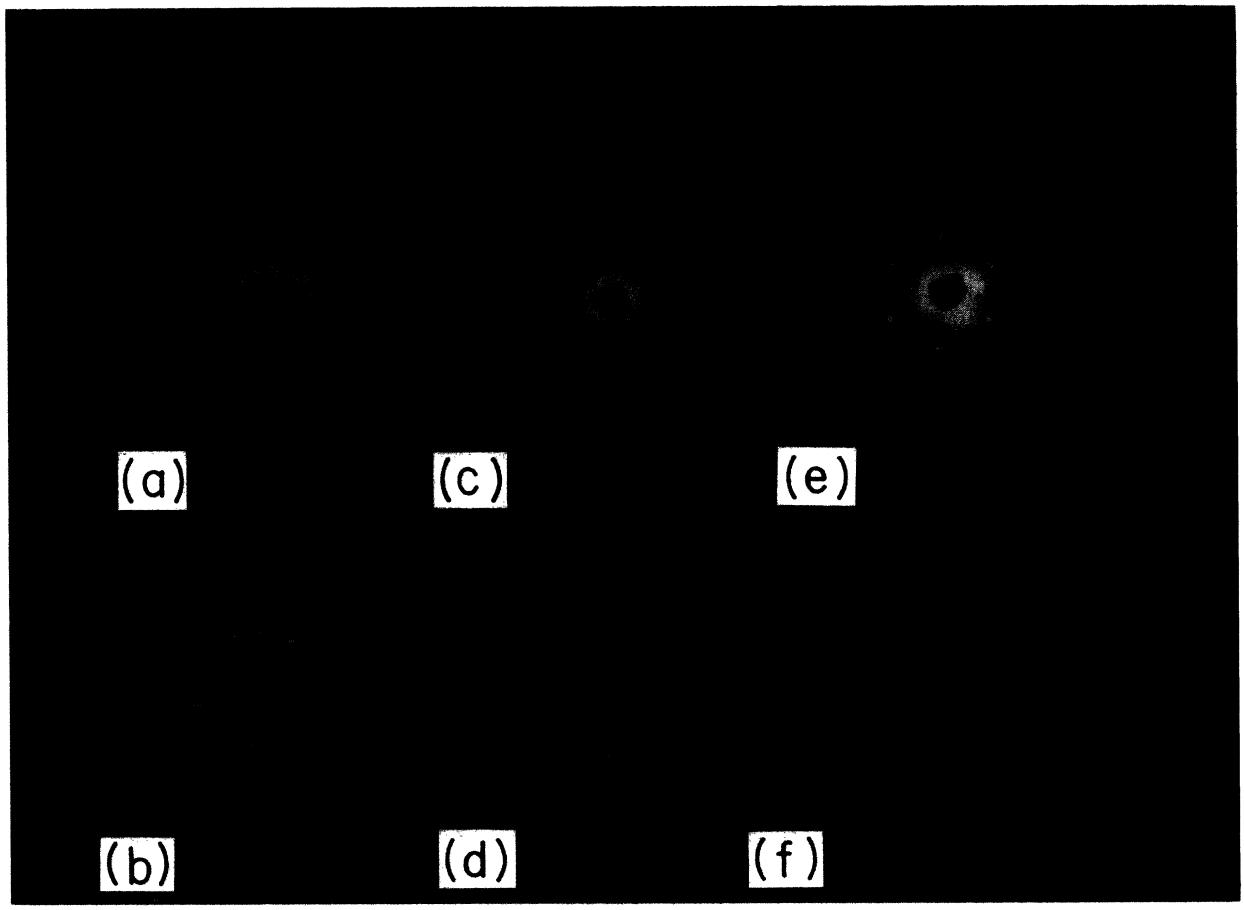

FIG. 2. Diffraction patterns from and real images of the colloid: (a) and (b), low-density single-layer fluid phase; (c) and (d), 1△ phase near the fluid phase; (e), 1△ phase near the hopping phase; and (f), transition region from 1△-hopping 2□. Black circles in the diffraction photographs are fiducial lines drawn on the translucent screen. In (a) the Debye-Scherrer ring is just inside the first fiducial circle. This corresponds to the disordered image in (b) which shows a gradient in planar density of spheres. Notice in (c) the hexagonal spots from the 1△ crystal are directly superimposed on the fluid Debye-Scherrer ring indicating continuity of density across the transition. An image of the very well-ordered single-layer crystal is shown in (d). In (e) most of the first-order spots are outside the calibration ring while in (c) most of the first-order spots are within the ring. This is a measure of the variation in $a_{\triangle}$ with D. In (f), showing the 1△-hopping-2□ phase transition, some spheres are less well focused than others due to their large vertical and horizontal motions. Second layer of spheres in the 2□ phase is in poor focus in this image. △ and □ regions are marked. Note, the black splotches in the images, most noticeable in (b), are due to dust in the optical path.

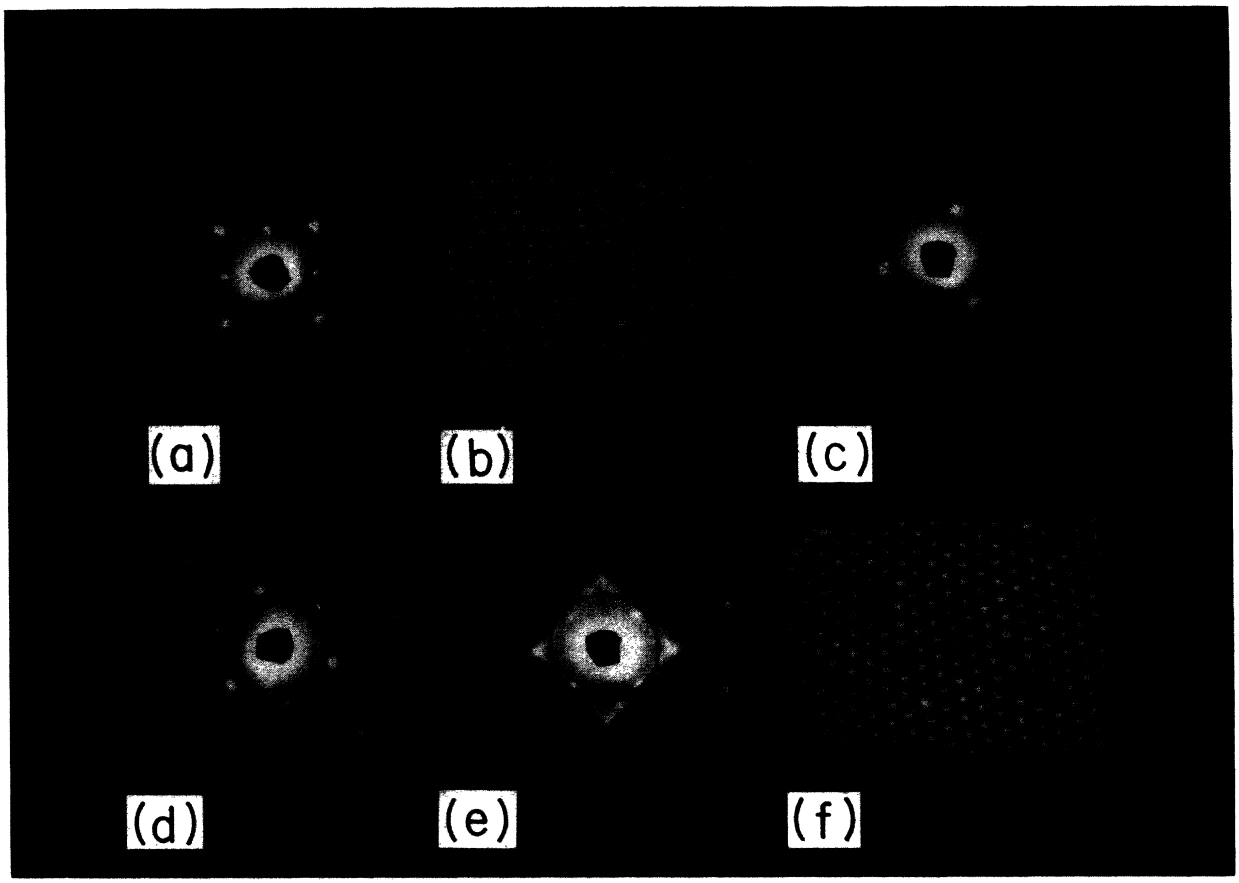

FIG. 3. Diffraction patterns from and real images of two and three layers of colloidal crystals: (a), diffraction from 2□; (b), image at the 2□–2△ boundary with the □ and △ phases indicated; (c), diffraction from 2△ near the 2□ boundary; (d), diffraction from 2△ near the 3□ boundary; (e), diffraction from the 3□ phase; and (f), image of the 3□–3△ transition. Notice the very distinct square symmetry in the 2□ phase in (a) and the almost perfect destructive interference of three of the first-order diffraction spots in the 2△ near 2□ in (c). In (d), the same three spots are not nearly as close to destructive interference as in (c), indicating a change in the ratio of $a_{\triangle}$ to vertical layer spacing. In (f), notice the very gradual transition from 3□–3△ and contrast it with the abrupt transition shown in (b) for the 2□–2△ transition. Diffraction photos have fiducial circles and images have □ and △ regions marked.

tion gear was added to the vertical fine focus gear of the microscope, and with this arrangement reproducible vertical adjustments of the microscope focus can be made to within the accuracy of the depth of focus of the objective, providing care is taken to avoid gear lag. This adjustment was necessary due to the unavoidable waviness of the bottom cover slip. Our measured statistical accuracy of the thickness measurement at one position in the cell is ± 0.15 μm, close to the depth of focus of the lens. However, systematic errors in thickness measurement with this technique are certainly possible and are probably comparable in size. For $\Phi = 0.305$ μm spheres with $a_s \approx 1.3$ μm it is possible to focus on as many as 20 consecutive layers of spheres before multiple scattering reduces the contrast to the point where it becomes impossible to distinguish individual layers. Multiple scattering from the spheres thus effectively makes both imaging and diffraction "surface" probes.

III. RESULTS

In Figs. 2–4, we show diffraction patterns and real-space images of a series of structural phases in a thin colloid wedge in the big cell. The diffraction patterns and images were obtained from the same crystallites by translating the cell along the wedge direction on both the diffraction stage and the microscope. All experimental runs described in this section were performed in the "clean," completely ion-exchanged limit, with the precleaned colloid in direct contact with ion-exchange resin. Under these experimental conditions, we can as a first approximation assume that the only shielding charges around the polystyrene spheres are the Z hydronium conterions. We will discuss the differences we find in the structural phases for "dirty" colloid with added electrolyte in a later section.

In the clean limit, we observe a sequence of structural phases quite similar to that observed by Pansu *et al.*[1] in a colloid system much closer to the hard-sphere limit of interactions. This sequence corresponds closely to that expected[13] for the packing of hard spheres at the high-pressure limit. The crystalline phases we observe alternate in □ and △ symmetry parallel to the bottom window surface in the sequence: 1△–2□–2△–3□– $\cdots$ for the first few phases, exactly like hard-sphere packings. The photo-

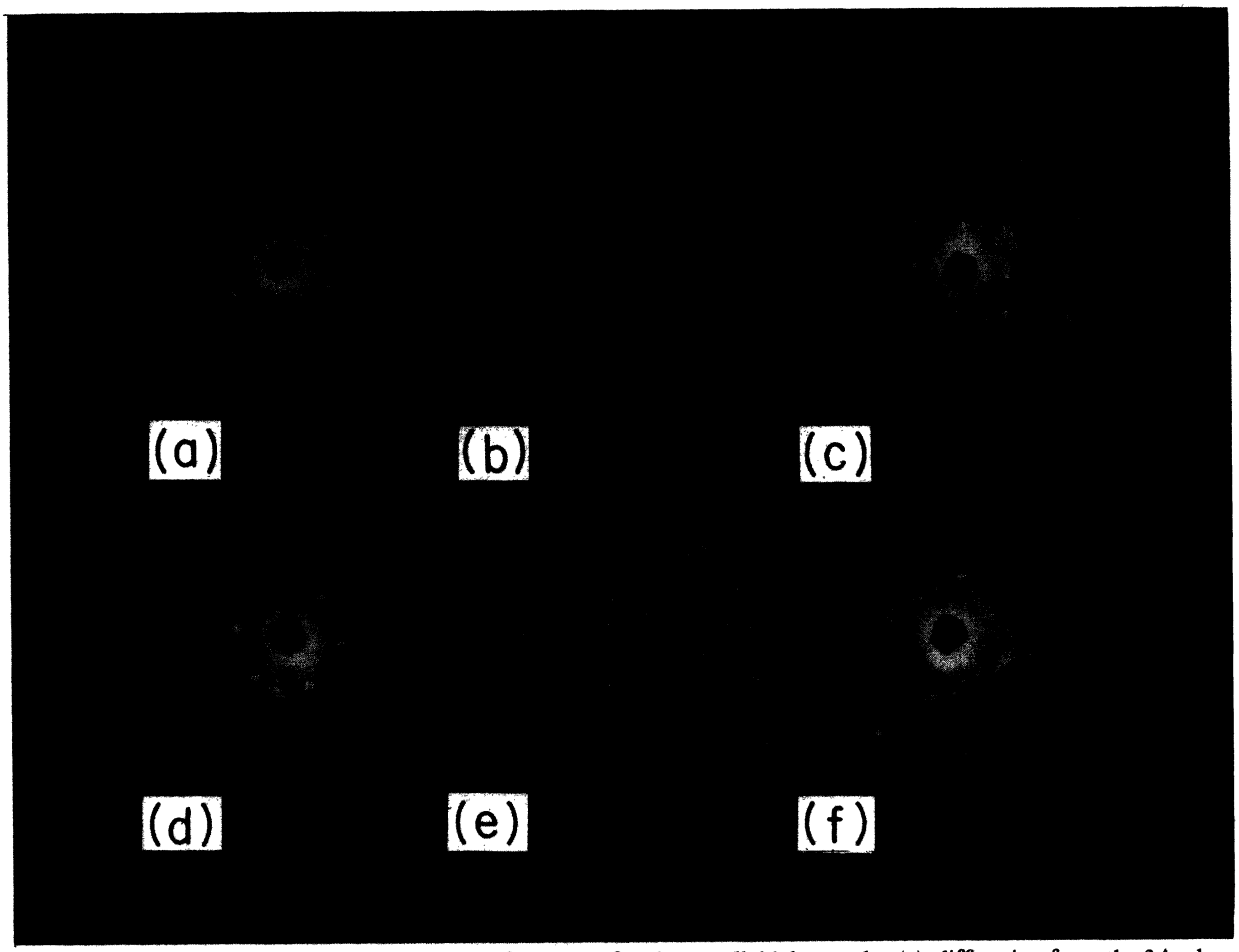

FIG. 4. Diffraction patterns from and real images of three- to five-layer colloidal crystals: (a), diffraction from the 3△ phase; (b), image of the 3△—4□ transition; (c), diffraction from the 4□ phase; (d), diffraction from the 4△ phase; (e), image of the 4△—5□ transition; and (f), diffraction from the 5□ phase. The diffraction patterns for 4□ and 5□ are strikingly different. This distinction is harder to discern in the images though it does exist, the 4□ image exhibits longer-range square symmetry than the image of 5□. This shows the distortions that occur in the square phases for $N \geq 4$, which mediate the $N\square$—$N\triangle$ transitions. The diffraction pattern in (f) begins to exhibit features of diffraction from a 3D bcc crystal with its ⟨110⟩ face parallel to the glass. Diffraction photos have fiducial circles and images have △ and □ regions marked.

graphs of real-space images of the colloid in Figs. 2—4 are taken of the first layer of spheres immediately above the bottom window, with 1-sec exposure. These are digitized images from video tape. The diffraction patterns in the figures were taken with 0.4745 μm (vacuum wavelength) light at normal incidence to the bottom window, also with one second exposure. One can observe in the figures the different symmetries of the crystal faces parallel to the glass as the thickness D increases in the wedge.

A. Comparison of the observed structural phases with those expected for the hard-sphere limit

In our system notable differences from the dense hard-sphere packings are found. The most obvious difference from the results of Pansu *et al.*[1] is the very low density of our colloid. In 3D, the colloid is observed to undergo a fcc-bcc phase transition for $a_s/\Phi > 3.6$ (Ref. 20) in the "clean" limit. The densities we have studied in the thin wedge span the range $2 < a_s/\Phi < 6$, thus our data on confined structures includes samples for which the stable bulk 3D crystal structure is both fcc and bcc. Phase diagrams of measured phase-transition points for ten different experimental runs are compared to calculated expected phase diagrams for hard spheres[13] in Figs. 5—8. Figures 5 and 7 contrast the two phase diagrams plotted as a function of the variables a_s/Φ and a_s/D. These are convenient parameters to use as $a_s/D \rightarrow 0$ is the limit of three dimensions. In Fig. 5 the transition points for each run are connected by dashed lines, and solid lines are drawn to connect the phase crossings. The largest statistical errors in the data and systematic variation noted for some runs in the positions of the phase crossings are due to the errors inherent in using the microscope with its relatively large depth of field to measure the wedge thickness, for $0.5 \leq D \leq 5$ μm. Error bars are not shown in Fig. 5, but have been included in the plot of the same observed phase crossing points as a function of a_s/Φ and D/Φ, in Fig. 6.

The hard-sphere high-pressure boundaries are shown in the Figs. 5—8. The forbidden regions in the phase diagrams are higher density than the highest-density pack-

ings possible for hard spheres between parallel hard plates at a certain ratio of sphere diameter to distance between the plates. Incomplete phase diagrams for hard spheres are shown in Figs. 7 and 8. In these figures, we have used calculations[13] of the high-pressure limit, highest-density packings of spheres with △ and □ symmetry without attempting to consider stability of the hard-sphere crystalline phases at lower densities (lower pressure). The limiting transition from the 3D fcc, hcp crystalline phase to fluid at $a_s/D=0$ and $a_s/\Phi=1.02$ is marked in Figs. 7 and 8. For the thin crystals one might expect a slightly larger region of crystalline stability in the low-density region $a_s/\Phi \geq 1$ for a_s/D close to unity compared with the 3D limit, $a_s/D \rightarrow 0$, as the plates impose vertical correlations on the spheres. However, the thin crystalline phases will eventually melt for $a_s/\Phi \geq 1.5$, possibly making a smooth transition from a fluid exhibiting vertical layering[21] to a fluid which is more isotropic. The striking distinction between our data and hard-sphere structures is that the hard-sphere layered phases would certainly be fluid at the large values of a_s/Φ we observe to be crystal-

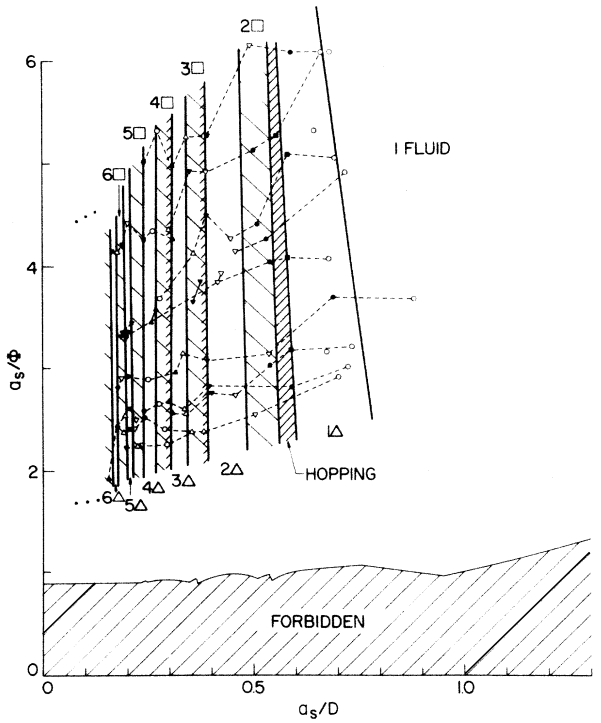

FIG. 5. Experimental transition points for ten different samples, showing a_s/Φ versus a_s/D. The separate runs are distinguished by the points connected by dashed lines. Phase transitions in each run are marked with different symbols. The symbols alternate between solid and open, with solid symbols marking the $N\triangle-(N+1)\square$ transitions. The continuous transition from 1△ to observable hopping (vertical fluctuations larger than the depth of focus of the objective) is marked on a few runs by solid squares. The run at $\sim 3 < a_s/\Phi < 3.5$ with two points for the same observed transition connected by solid lines shows the different values for a_s deduced from measurements on the square phase versus measurements on the neighboring hexagonal phase. Solid lines separating the phases are approximations obtained by eye, connecting like points within the scatter. The hopping regions observed near $N\triangle-(N+1)\square$ transitions are shaded. The indicated forbidden region is bounded above by the closest packed high-pressure limit, assuming hard-sphere interactions with sphere diameter 0.305 μm. Within experimental accuracy, the phase-transition lines extend downward to meet the high-density hard-sphere phase transitions (see also Fig. 7). Presumably a fluid region exists at low density above the lowest-density runs which we performed ($a_s/\Phi \approx 6$). We have not explored this region of phase space. The void region exists somewhere to the right of the fluid region in the phase diagram. In the hard-sphere high-pressure limit there is no fluid region, and the void region starts at $a_s/D=a_s/\Phi=0.953$.

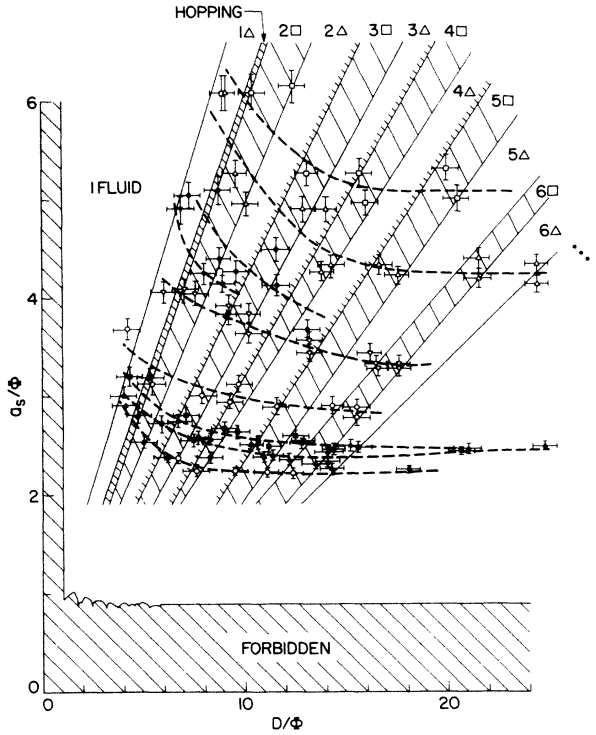

FIG. 6. The experimental transition points of Figure 5 now showing the phase diagram of the thin colloid system plotted as a_s/Φ versus D/Φ. The error bars take into account statistical measurement inaccuracies, most of which are due to the measurement of D, as discussed in the text. Solid lines are shown approximately connecting the phase boundaries for individual runs. The 2D fluid region, bounded by the leftmost point in each run, seems to connect continuously to the high-pressure, hard-sphere limit at the lower left, $a_s/\Phi=0.953$, $D/\Phi=1$, with zero width. The thick dashed lines are a guide to the eye connecting like points from the same run. For clarity, the two highest-density runs share a single curve. The actual lines in the phase diagram following a single run are expected to exhibit more structure, due to the density variations within each phase, as discussed in the text. These variations are probably a significant cause of the scatter in the values of a_s/Φ about the dashed lines. The slope of each curve is in some sense a measure of the compressibility of the thin colloidal crystal for each specific experimental run. Notice that for constant D/Φ the crystals with larger values of a_s/Φ have steeper slopes, and therefore larger compressibilities. Also note that, as a result of this large compressibility for $N<3$, the experimental data do not scale to the hard-sphere high-pressure limit with a larger effective hard-sphere diameter (see Fig. 8).

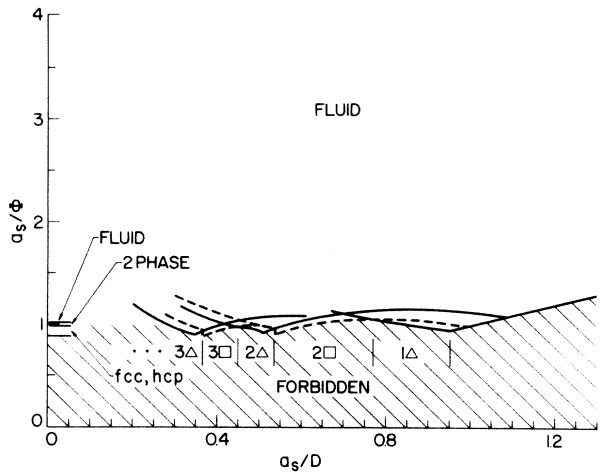

FIG. 7. Partial theoretical phase diagram for a hard-sphere system confined by two parallel hard surfaces, using the calculations of Ref. 13, plotted using the variables a_s/Φ and a_s/D as in Fig. 5. Solid lines delimit the hexagonally packed phases and dashed lines delimit the square phases. The regions of higher density than these limits are forbidden. As in Ref. 13, it is assumed that in the high-density limit, the equilibrium structure at any value of a_s/D is the one with highest density. The anticipated transition points for the hard-sphere high-pressure system confined by hard surfaces are marked by vertical lines. Phase boundaries for the 3D limit $a_s/D \to 0$ are shown at left. For values of $a_s/D \gg 1$, the thin hard spheres must melt to a fluid, possibly through an intermediate layered fluid phase.

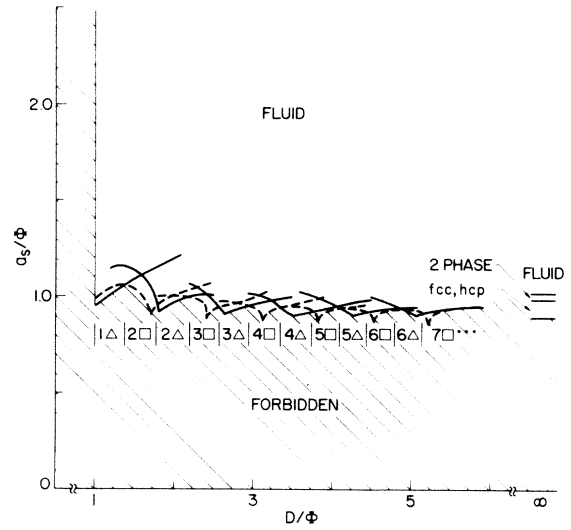

FIG. 8. Partial theoretical phase diagram of the hard-sphere system confined between two parallel hard surfaces of Ref. 13 and Fig. 7, but plotted as a_s/Φ versus D/Φ for comparison to the experimental phase diagram in Fig. 6. Phase boundaries for the 3D limit $D/\Phi \to \infty$ are shown at right. The void region, $D/\Phi < 1$, is shown as forbidden, as well as the regions of higher density than the highest-density packings. These are delimited by solid and dashed lines for triangular and square symmetry parallel to the boundaries, respectively. The anticipated transition points for the hard-sphere high-pressure system confined by hard surfaces are marked by vertical lines as in Fig. 7. For values of $a_s/\Phi \gg 1$, the confined hard spheres must melt to a fluid.

line. In addition, our data do not scale to the hard-sphere limit using an effective hard-sphere diameter.

1. One-layer fluid. We find a 3D fluid phase with density varying inversely with thickness at very small D/Φ that in theory does not exist for hard spheres at the high-pressure limit. The Debye-Scherrer ring from the 2D fluid is apparent in the first two diffraction patterns in Fig. 2. Time-dependent angular correlations in the diffraction pattern of the 2D fluid phase have previously been observed[22] in a thin colloidal system of 0.2-μm-diameter spheres at low density. A gradual transition occurs from this 2D fluid to the 1△ hexagonal solid as D is increased. The image of the 2D fluid shows rather low density, fast moving spheres with six-fold coordination on the average. Imaging the colloid as it undergoes the 2D fluid-solid transition is currently underway and will be reported elsewhere.[20] In the measured phase diagram in Fig. 6, one observes that the 2D fluid and the 1△ 2D solid transition line connecting the first points for each run, within experimental accuracy, extrapolates to the hard-sphere limit of $a_s/\Phi = 0.953$, $D/\Phi = 1$. The 2D fluid phase has no width at $a_s/\Phi = 0.953$ (does not exist at the high-pressure limit) and opens up monotonically as the density is decreased.

2. $N = 1-3$. The general structure of one to three layers of crystallized spheres in our low-density, clean system is a similar sequence of 1△–2□–2△–3□–3△ phases as those reported by Pansu *et al.*[1] but with important differences. In the hard-sphere system at high pressure[13] the 2D sphere separation does not vary as D is changed. In contrast, particularly for the one- and two-layer structures, we observe dramatic variations in $a_\triangle$ and $a_\square$ the nearest-neighbor distances in the XY plane for the hexagonal and square phases, respectively. These variations are obvious in the diffraction photos for 1△ and 2△ shown in Figs. 2 and 3, respectively. Figure 2(c) shows the hexagonal spot pattern of the 1△ phase superimposed on the Debye-Scherrer ring of the scattering from the single-layer fluid phase. Both appear in the diffraction pattern because the focus of the laser beam spans the two phases. In another experiment Clark *et al.*[22] used a 5-μm-diameter laser beam waist illuminating only ~25 spheres and probed the correlations in the fluid region near the 2D fluid to solid transition, observing transitory hexagonal symmetry. We focused the laser to a 30-μm-diameter beam waist, thereby probing almost two orders of magnitude more of spheres and obtaining a space and time-averaged diffraction pattern. Comparing Fig. 2(c) with 2(e) the diffraction pattern of the 1△ phase near the 2□ boundary, we see that the first-order diffracted spots are on a circle of distinctly larger radius in Fig. 2(e). A similar observation is made for the 2△ phase in Figs. 3(c) and 3(d). The increase in radius is a measure of the decrease in $a_\triangle$ as thickness increases, thereby keeping the volume density relatively constant. We have found that in the 1△ phase at large a_s/Φ, $a_\triangle$ can vary by as much as 40% from the one-layer fluid boundary to the 2□ boundary. This indicates that the 2D colloidal crystal is more compressible than a hard-sphere crystal. At the 1△–2□ boundary, we find $a_\square$ to be as large as $1.2a_\triangle$. For hard-sphere packings,[13] the △ and □ structures have the same

value for $a_\triangle$ and $a_\square$. As $a_s/\Phi \to 2$ in our experiments, the variation of $a_\triangle$ and $a_\square$ is much smaller. Pansu *et al.*[1] observe no change in $a_\triangle$ and $a_\square$ for $1.4 < a_s/\Phi < 1.9$. Clearly the distortions we observe at low densities are a reflection of the softness of these colloidal crystal structures. Colloidal crystals in 3D have elastic compliances $E \approx 1$ cm^2/dyn (Ref. 23) nine orders of magnitude larger than for atomic or molecular crystals, due to the weak interactions stabilizing these structures.

In both of the $2\triangle$ diffraction patterns shown in Figs. 3(c) and 3(d) we notice a distinct threefold symmetry. The near cancellation of the $\langle 11 \rangle$, $\langle 1\bar{1} \rangle$, and $\langle \bar{1}0 \rangle$ spots is caused by the phase difference between the scattering from the two planes of spheres separated vertically by $\frac{1}{2}a_\triangle$. This is analogous to the destructive interference from the $\langle 110 \rangle$ planes in the diffraction from a bcc lattice.[24] The interplane order is closer to perfect *ab* stacking near the $2\square$ boundary, yielding almost perfect destructive interference for Fig. 3(b). The increase in intensity of these spots as the $2\triangle$ phase is traversed along the wedge indicates that the interlayer stacking is increasing and possibly becoming distorted from that for an unstressed crystallite as the thickness increases. Near the $3\square$ boundary the $2\triangle$ crystallite is sheared, there is considerable vertical hopping, and it no longer exhibits perfect *ab* stacking.

These observed variations in $a_\triangle$ and $a_\square$ lead naturally to the discussion of colloid volume density in the thin phases. For the $\square$ phases the volume density is defined to be $a_s^{-3} \equiv N/(a_\square^2 D)$, while for the $\triangle$ phases it is $a_s^{-3} \equiv 2N/(\sqrt{3}a_\triangle^2 D)$. The volume density of spheres decreases to zero in the void region, where D/Φ is too small to allow spheres between the plates. Within the accuracy of our measurement the volume density of spheres increases rapidly when D/Φ becomes large enough to admit spheres, then increases slowly to a maximum at the fluid-$1\triangle$ boundary, and decreases on the order of 5% as D/Φ increases within the $1\triangle$ phase to the $2\square$ boundary. The experimental error in the measurement of D swamps any noticeable variation in volume density in a single phase for $N > 1$. However, we do observe a dramatic decrease in a_s/Φ between phases as thickness is increased, as shown in Fig. 6. This effect is much more pronounced for the larger values of a_s/Φ.

The phase diagram for hard spheres is shown in Fig. 8, plotted as in Fig. 6, but on a different horizontal scale. From Fig. 8, one can observe significant fluctuations in the actual values of a_s/Φ within any one phase for the hard spheres as the thickness varies. These were noted by Pansu *et al.*,[1] for the larger colloidal spheres. We expect similar fluctuations in a_s/Φ within the low-density colloidal phases but this requires more careful study. To obtain the data shown in Fig. 6, we measured the transition points between phases for each different colloidal sample. The error bars reflect the errors in measurement and are not an estimate of the fluctuations in a_s/Φ expected within a given phase. We expect that as a_s/Φ becomes larger the interactions between spheres becomes weaker, thus the variation in a_s/Φ with D/Φ within any single structural phase probably increases from that for hard spheres as a_s/Φ increases. It is possible this expected variation leads to some of the scatter in the data plotted in Fig. 6.

With increasing thickness we first notice for $N = 3$ that the $\triangle$ phases exhibit only hcp stacking in the clean limit, even for a_s/Φ as low as 2. The hcp stacking of $\triangle$ phases persists for crystals as thick as ten layers. This is quite different from the case of Pansu *et al.*,[1] who observed roughly equal proportions of hcp and fcc stacking, as expected for hard spheres. In our case, the symmetric stacking for small N is a manifestation of relatively strong sphere-sphere and sphere-wall interactions.

3. $N \geq 4$. Above three layers there is a qualitative difference in the observed structural distortions with increasing D within a phase compared with those observed for $N < 4$. For small N we see a pronounced variation of $a_\triangle$ and $a_\square$ in a single phase and also between phases as D increases. For $N \geq 4$ we no longer discern any variation in $a_\triangle$ or $a_\square$. We observe hopping regions at the boundaries of $N\triangle - (N+1)\square$, but as N increases these fluctuations in Z in any one layer become difficult to discern. For small N we observe that the $N\square - N\triangle$ transition occurs as a smooth distortion of the square symmetry into the hexagonal over a small number of lattice sites (< 20). With increasing N we observe much broader distorted regions, in fact in some cases the $N\square$ phase is distorted into twofold symmetry parallel to the plates even at the $(N-1)\triangle - N\square$ transition. This is observed in the microscope image in Fig. 4(e) as a distortion of the lattice from the right angles of the square phases. In this case more information is obtained from diffraction, where we observe that the second-order diffraction spots approach the symmetry of a 3D bcc crystal, Fig. 4(f).

The diffraction from a 3D bcc crystal with the $\langle 110 \rangle$ face perpendicular to the incident wave vector has the same four second-order spots as those in Fig. 4(f) but none of the first-order $\langle 100 \rangle$ spots due to exact cancellation. The cancellation is not complete in the confined system of a small number of layers for several possible reasons: The crystal lattice may be strained near the glass surfaces; we have observed the layer spacings to change with D. We cannot measure the vertical spacings accurately enough to determine if there is a difference between the layer spacings nearest the walls and the spacings farthest from the walls for $N \geq 4$. For odd N or small N there cannot be exact cancellation of the $\langle 100 \rangle$ spots. There may also be stacking faults within the scattering volume, and possible shear induced by the walls of the wedge.

B. Dirty systems

We have been able to distinguish differences in the structural characteristics of the colloidal crystals in clean or dirty wedges. In very clean wedges with $2 < a_s/\Phi < 6$, we observe that the hexagonally symmetric phases characteristically exhibit hcp packing. It is unclear why hcp stacking is preferred in these $\triangle$ phases. This preference usually indicates a strong next-nearest-neighbor interaction in 3D systems.[25] In our system, the glass surfaces impose hexagonal symmetry while the bulk energetics prefer bcc, for $a_s/\Phi \geq 3.5$. We do not observe a change in this observed hcp stacking for $a_s/\Phi < 3.5$. However, in

dirty systems when it is clear that the system is contaminated by stray ions, we observe a mixture of fcc and hcp stacking for the △ phases.

In dirty systems the square phases are observed to be considerably less stable than the hexagonal phases. In a crystal which degraded over time, possibly due to an air leak in the cell, we observed that the square phases disordered into fluid while the hexagonal phases were still stable. We can induce local stray ion concentrations in our cells by heating with the incident microscope illumination, sometimes in spite of good infrared and ultraviolet filters reducing those components by ≈ 8 orders of magnitude. When this heating occurs the square phases always melt before the hexagonal phases. When the system originally crystallizes the hexagonal phases also stabilize first, with the square phases stabilizing as much as a day later.

C. Hopping

The transitions from $N\triangle-(N+1)\square$ are not abrupt in the clean or dirty colloidal system. Particularly, the first transition from $1\triangle-2\square$ in a sample with gentle enough wedge angle is extremely interesting. For high sphere densities near $a_s/\Phi \geq 1$, Ogawa[14] reported an observation by Hachisu of a two-layer mazelike pattern of spheres, stable for plate separation slightly larger than stabilizes a single layer of spheres and slightly less than stabilizes two layers of close-packed spheres in an ordered lattice. We observe this same occurrence for values of $a_s/\Phi < 2$. Pieranski *et al.*[1] reported fluctuations in the vertical motion of 1.1-μm-diameter spheres as the transition is approached from the $1\triangle$ side for $a_s/\Phi < 2$. For $a_s/\Phi > 2$ we observe a hopping region in which the spheres, seemingly at random, hop between two stable positions, closer to either the top or the bottom plate that eventually separate vertically into the two layers of the $2\square$ phase. The hopping frequency is on the order of 0.1 to 10 Hz, allowing easy observation of the correlations and anticorrelations in the hopping of neighboring spheres in the image of the system. Focusing the microscope in the preferred plane closer to either surface we observe a continuous evolution with increasing D, from just a few spheres hopping out of the single-layer hexagonal lattice ($1\triangle$) to on the order of half the spheres hopping into and out of focus. It would be interesting to study this system as the possible manifestation of a 2D Ising model.[1,14] In the hopping regions we observe the lattice to become quite distorted from either the △ or □ structures, as seen in Fig. 1(f). This is a manifestation of large amplitude dynamical horizontal motions in conjunction with the vertical hopping. The boundary of the hopping region close to the stable $2\square$ region is characterized by lack of long-range correlations in the XY plane. There seems to be a continuous variation between transitory hexagonal and square structure as observed in the plane. We also observe similar fluctuations in vertical positions of spheres in the hexagonal phases near others $N\triangle-(N+1)\square$ transitions, but these are less striking as the vertical fluctuations are spread between several layers.

IV. CONCLUSIONS

We have made use of both diffraction and real-space lattice imaging to characterize the structural phases observed for colloidal crystals undergoing the transition between 2D and 3D for a wide range in densities. We have been particularly careful to keep the system very free from ionic contamination, noticing distinct differences in the structures observed in clean and dirty cells. We find a similar series of structural phases in the clean system as expected in the hard-sphere limit, but with notable differences from the details of the hard-sphere structures. Although in 3D our crystals are observed to undergo a bcc-fcc phase transition for densities such that $a_s/\Phi \leq 3.5$, we do not observe a dramatic structural change in the thin clean colloidal crystals in the range $2 < a_s/\Phi < 6$. We do observe qualitative differences in a dirty system with added electrolyte.

The layering transitions and structural phases observed are examples of the rich and complex behavior of a rather simple real system. It should be possible to map out the phase diagram experimentally and understand it theoretically in detail. The clean experimental phase diagrams we have shown in Figs. 5 and 6 comprise one small part of a complex three-parameter phase diagram, which would include another parameter involving electrolyte screening, for example, a_s/λ. Note that the paths we have mapped out in the clean system would not fall on a single plane were this other parameter included, since λ is a function of a_s in the clean limit. It will be interesting to study this large phase diagram in detail to determine whether any of several recently proposed[2,26–28] model interaction potentials for colloidal spheres are consistent with experiment.

ACKNOWLEDGMENTS

We wish to thank C. C. Grimes for encouragement, helpful discussions and the use of the microscope in his office. We also had invaluable assistance from D. Kwo, a participant in the AT&T Bell Laboratories Summer Research Program.

[1]Pa. Pieranski, L. Strzlecki, and B. Pansu, Phys. Rev. Lett. **50**, 900 (1983); and B. Pansu, P. Pieranski, and L. Strzelecki, J. Phys. **44**, 531 (1983).

[2]Pa. Pieranski, Contemp. Phys. **24**, 25 (1983).

[3]For example, manufactured by the Dow Chemical Company, Midland, Michigan.

[4]A. Homola and R. O. James, J. Colloid Interface Sci. **59**, 123 (1977).

[5]R. Williams and R. Crandall, Phys. Lett. A **48**, 225 (1974).

[6]A. Kose, M. Ozaki, K. Takano, Y. Kobayashi, and S. Hachisu J. Colloid Interface Sci. **44**, 330 (1973).

[7]E. J. W. Verwey and J. Th. G. Overbeek, *Theory of the Stability of Lyophobic Colloids* (Elsevier, New York, 1948).

[8]B. J. Alder, W. G. Hoover, and D. A. Young, J. Chem. Phys. **49**, 3688 (1968).

[9]M. Baus and J.-P. Hansen, Phys. Rep. **59**, 1–94 (1980).

[10]P. M. Chaikin, P. Pincus, S. Alexander, and D. Hone J. Colloid Interface Sci. **89**, 555 (1982).
[11]A. A. Kamel, M. S. El-Asser, and J. W. Vanderhoff, Dispersion Sci. Technology **2**, 183 (1981).
[12]R. K. Iler, *The Chemistry of Silica* (Wiley, New York, 1979), p. 358.
[13]B. Pansu, Pi. Pieranski, and Pa. Pieranski, J. Phys. **45**, 331 (1984).
[14]T. Ogawa, J. Phys. Soc. Jpn. **52**, 167 (1983).
[15]See, for example, L. D. Marks, *Structure and Dynamics of Surfaces,* edited by P. von Blackenhagen and W. Schommers (Springer-Verlag, New York, 1986); and J. A. Venables, Ultramicroscopy **7**, 81 (1981).
[16]G. Binnig, H. Rohrer, Ch. Gerber, and E. Weibel, Phys. Rev. Lett. **49**, 57 (1982).
[17]A. J. Hurd, N. A. Clark, R. C. Mockler, and W. J. O'Sullivan, Phys. Rev. A **26**, 2869 (1982).
[18]We are indebted to T. A. Palumbo of AT&T Bell Laboratories for providing us with the gold electroplating.
[9]Equal parts of Fisher Rexyn 101 and 201 cation and anion exchange resin are used, and cleaned by a series of acid and base rinses in the manner of the J. W. Vanderhoff, H. J. van den Hul, R. J. M. Tausk, and J. Overbeek, in *Clean Surfaces,* edited by G. Goldfinger (Dekker, New York, 1970).
[20]C. A. Murray and D. H. Van Winkle (unpublished).
[21]I. K. Snook and D. Henderson, J. Chem. Phys. **68**, 2134 (1978).
[22]N. A. Clark, B. J. Ackerson, A. J. Hurd, Phys. Rev. Lett. **50**, 1459 (1983).
[23]R. Williams, R. S. Crandall, and P. J. Wojtowicz, Phys. Rev. Lett. **37**, 348 (1976).
[24]See, for example, C. Kittel, *Introduction to Solid State Physics* (Wiley, New York, 1976), p. 58.
[25]R. Bruinsma and A. Zangwill, Phys. Rev. Lett. **55**, 214 (1985).
[26]S. Alexander, P. M. Chaikin, P. Grant, G. J. Morales, P. Pincus, and D. Hone, J. Chem. Phys. **80**, 5776 (1984); D. Hone, S. Alexander, P. M. Chaikin, and P. Pincus, *ibid.* **79**, 1474 (1983).
[27]I. Sogami, Phys. Lett. **96A**, 199 (1983).
[28]L. Guldbrand, B. Jonsson, H. Wennerstrom, and P. Linse, J. Chem. Phys. **80**, 221 (1984).

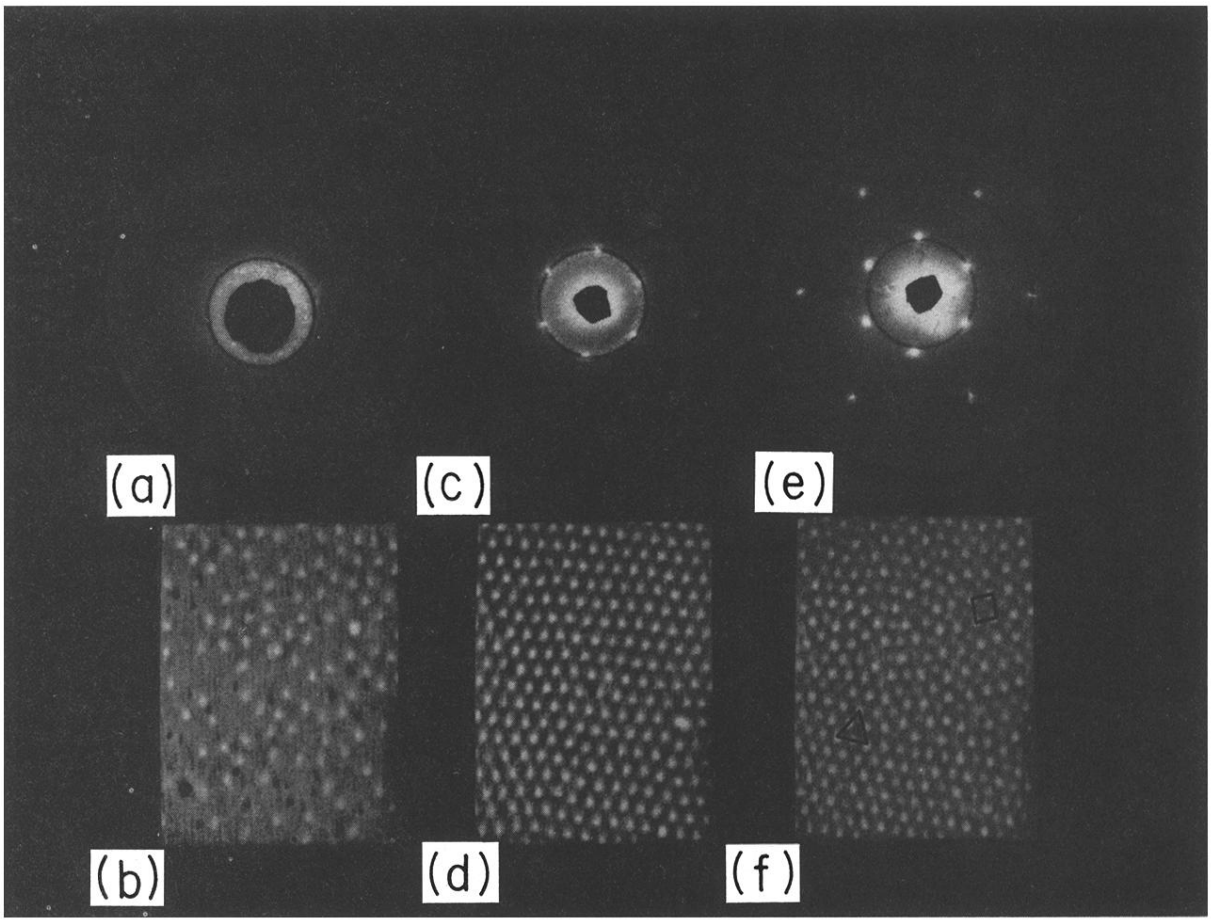

FIG. 2. Diffraction patterns from and real images of the colloid: (a) and (b), low-density single-layer fluid phase; (c) and (d), 1△ phase near the fluid phase; (e), 1△ phase near the hopping phase; and (f), transition region from 1△-hopping 2□. Black circles in the diffraction photographs are fiducial lines drawn on the translucent screen. In (a) the Debye-Scherrer ring is just inside the first fiducial circle. This corresponds to the disordered image in (b) which shows a gradient in planar density of spheres. Notice in (c) the hexagonal spots from the 1△ crystal are directly superimposed on the fluid Debye-Scherrer ring indicating continuity of density across the transition. An image of the very well-ordered single-layer crystal is shown in (d). In (e) most of the first-order spots are outside the calibration ring while in (c) most of the first-order spots are within the ring. This is a measure of the variation in $a_{\triangle}$ with D. In (f), showing the 1△-hopping-2□ phase transition, some spheres are less well focused than others due to their large vertical and horizontal motions. Second layer of spheres in the 2□ phase is in poor focus in this image. △ and □ regions are marked. Note, the black splotches in the images, most noticeable in (b), are due to dust in the optical path.

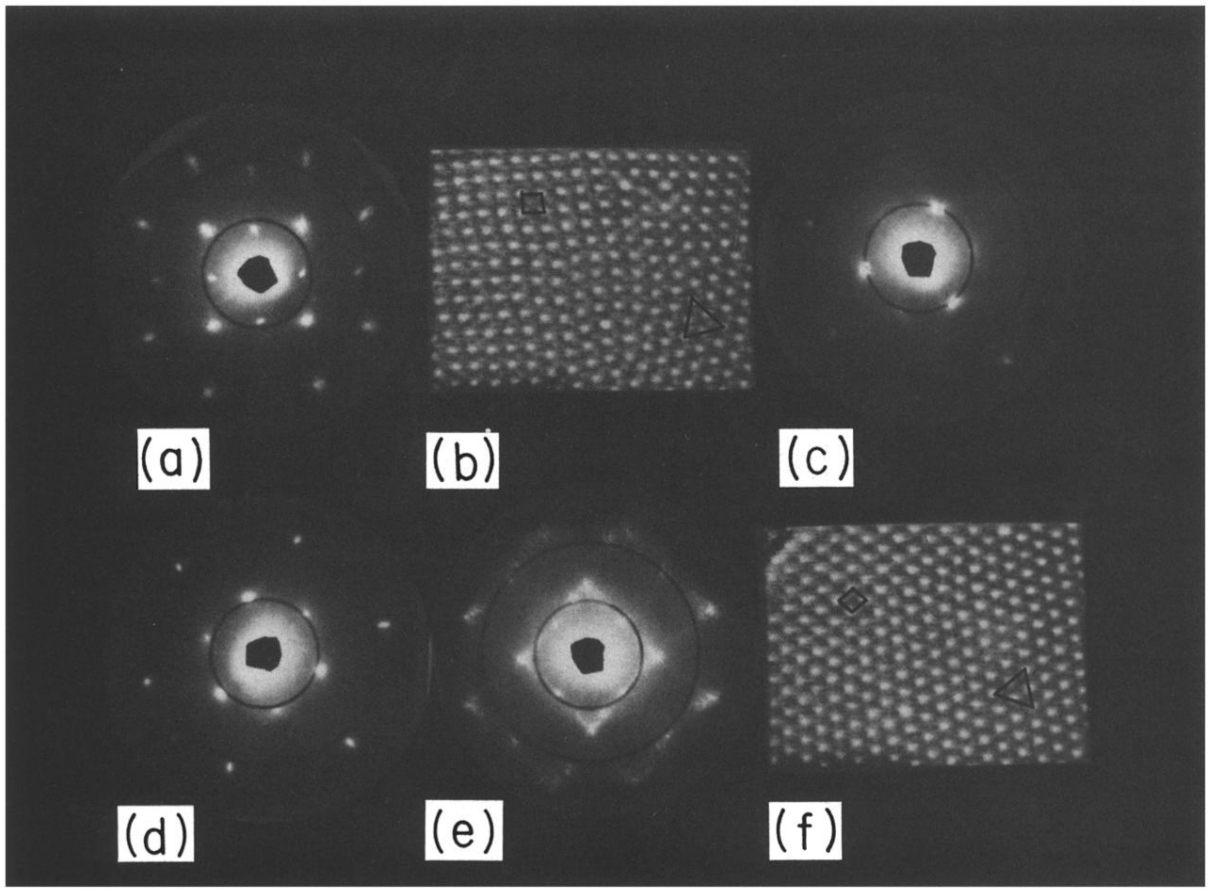

FIG. 3. Diffraction patterns from and real images of two and three layers of colloidal crystals: (a), diffraction from 2□; (b), image at the 2□–2△ boundary with the □ and △ phases indicated; (c), diffraction from 2△ near the 2□ boundary; (d), diffraction from 2△ near the 3□ boundary; (e), diffraction from the 3□ phase; and (f), image of the 3□–3△ transition. Notice the very distinct square symmetry in the 2□ phase in (a) and the almost perfect destructive interference of three of the first-order diffraction spots in the 2△ near 2□ in (c). In (d), the same three spots are not nearly as close to destructive interference as in (c), indicating a change in the ratio of $a_{\triangle}$ to vertical layer spacing. In (f), notice the very gradual transition from 3□–3△ and contrast it with the abrupt transition shown in (b) for the 2□–2△ transition. Diffraction photos have fiducial circles and images have □ and △ regions marked.

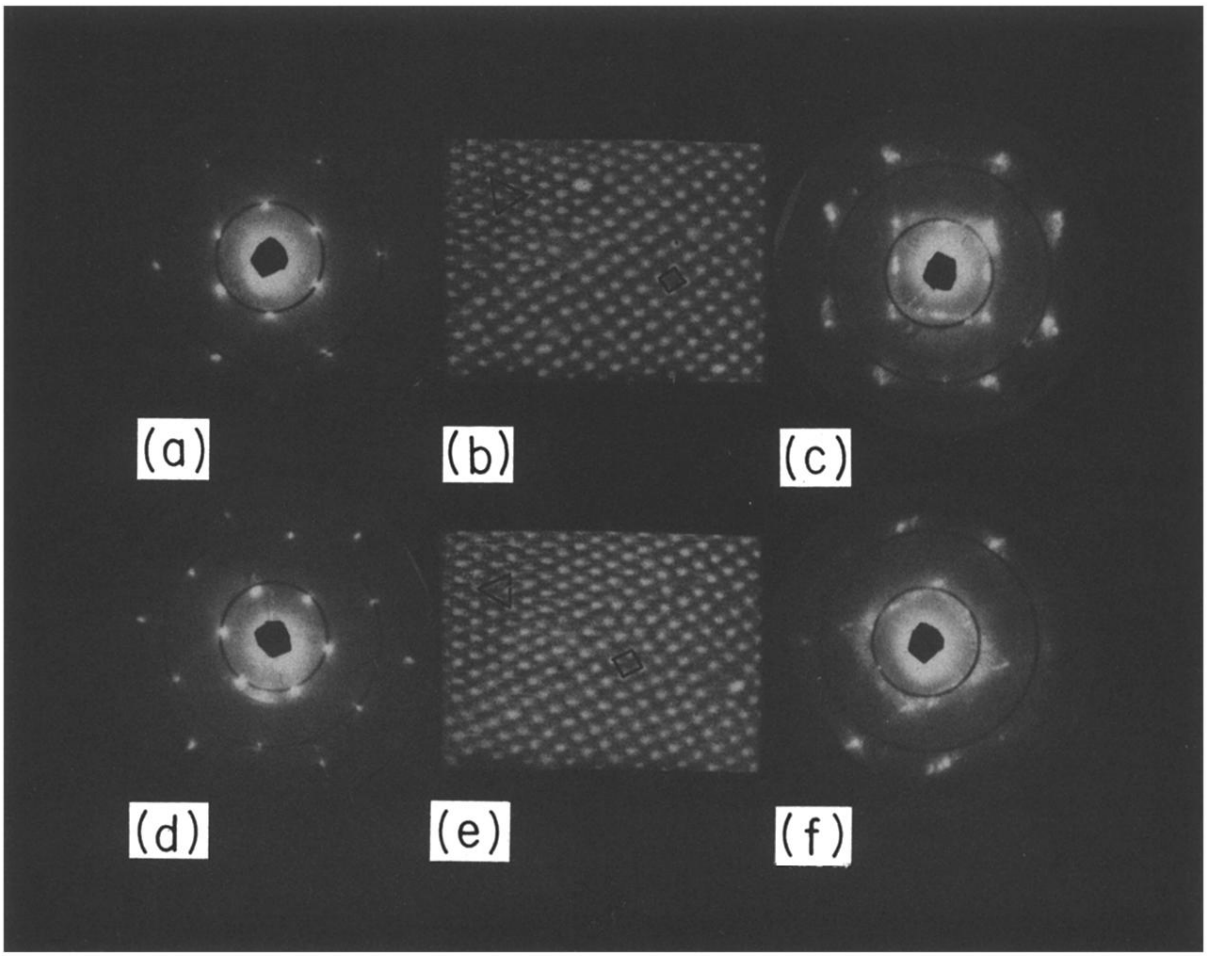

FIG. 4. Diffraction patterns from and real images of three- to five-layer colloidal crystals: (a), diffraction from the 3△ phase; (b), image of the 3△—4□ transition; (c), diffraction from the 4□ phase; (d), diffraction from the 4△ phase; (e), image of the 4△—5□ transition; and (f), diffraction from the 5□ phase. The diffraction patterns for 4□ and 5□ are strikingly different. This distinction is harder to discern in the images though it does exist, the 4□ image exhibits longer-range square symmetry than the image of 5□. This shows the distortions that occur in the square phases for $N \geq 4$, which mediate the $N\square$—$N\triangle$ transitions. The diffraction pattern in (f) begins to exhibit features of diffraction from a 3D bcc crystal with its $\langle 110 \rangle$ face parallel to the glass. Diffraction photos have fiducial circles and images have △ and □ regions marked.